



Realizing Nanoscale Quantitative Thermal Mapping of Scanning Thermal Microscopy by Resilient Tip-Surface Contact Resistance Models

Journal:	<i>Nanoscale Horizons</i>
Manuscript ID	NH-COM-02-2018-000043.R2
Article Type:	Communication
Date Submitted by the Author:	23-Apr-2018
Complete List of Authors:	Li, Yifan ; The University of Akron, Department of Chemical and Biomolecular Engineering Mehra, Nitin; The University of Akron, Chemical and Biomolecular Engineering Ji, Tuo; The University of Akron, Department of Chemical and Biomolecular Engineering Zhu, Jiahua; The University of Akron, Chemical and Biomolecular Engineering

Conceptual Insights

Existing scanning thermal microscopy (SThM) has unique capability to probe qualitative thermal properties of surfaces but quantitative techniques are not available yet due to the presence of unpredictable thermal contact resistance (TCR) at tip/substrate interface. In this work, we developed two mathematical models, linear and non-linear, those can be used to quantitatively describe the TCR for a variety of surfaces. The developed models bridge heat transfer across tip/surface interface and enable continuum thermal analysis. This work extends the capability of SThM in quantitative measurement and enables a unique platform for thermal measurement at nanometer spatial resolution, which opens up the opportunities to study quantified thermal properties across composite interfaces, multi-layer structures, photovoltaic devices, microelectronics, *etc.*

Realizing Nanoscale Quantitative Thermal Mapping of Scanning Thermal Microscopy by Resilient Tip-Surface Contact Resistance Models

Yifan Li, Nitin Mehra, Tuo Ji and Jiahua Zhu*

Intelligent Composites Laboratory, Department of Chemical and Biomolecular Engineering,
The University of Akron, Akron, OH 44325 USA

Corresponding Author: J. Z. E-Mail: jzhu1@uakron.edu. Tel: 1-(330)972-6859.

Abstract

Quantitative assessment of thermal property by scanning thermal microscopy (SThM) is a demanded technology but still not available yet due to the presence of unpredictable thermal contact resistance (TCR) at tip/substrate interface. TCR is mainly affected by three major interfacial characteristics including surface roughness, hardness and contacting force. In this work, TCR is mathematically derived into linear and non-linear models based on the interfacial micro-characteristics. The models have the capability to predict TCR for both rough and smooth surfaces with satisfactory accuracy. With predictable TCR, the heat transport across the tip/substrate nanointerface can be precisely described and thus quantitative thermal properties can be predicted from SThM measurement. The models are tested in three polymeric material systems, PDMS, epoxy and PVA. Thermal conductivity from model prediction matches very well (<10% error) to the measured values from bulk polymer samples. Such models use general surface feature as inputs, so it has wide applicability to other similar materials especially polymers. Moreover, the model has been tested valid in doped PVA samples when extrapolated to predict thermal conductivity beyond the range of model development. This work extends the capability of SThM in quantitative measurement and enables a unique platform for thermal conductivity measurement at nanometer spatial resolution.

Key Words: Scanning thermal microscopy, thermal contact resistance (TCR), thermal conductivity, quantitative measurement.

1. Introduction

The rise of nanotechnology and rapid development of microelectronics industry pose ever-increasing challenge of heat dissipation at micro-/nano-scale.^{1, 2} Effective cooling demands materials with excellent heat conduction capability. Besides the wide spreading technologies of making thermally conductive materials, precise and convenient measurement of thermal conductivity is still a big challenge in the field especially with materials down to micro-/nano-scale. In general, thermal conductivity can be measured by two different methods: steady state method and transient method.³⁻⁵ Steady state techniques are typically useful for bulk materials, which are developed based on the Fourier's law. The measurement requires an equilibrium system and thus it is usually time-consuming. Transient methods are less time consuming since the measurement is completed before system equilibrium.⁶ More importantly, requirement of sample dimension is less limited with transient techniques that enables thermal conductivity measurement at micron-scale. Over past decades, a few transient techniques have been developed including scanning thermal microscopy (SThM), time-domain thermoreflectance (TDTR), time-domain differential raman (TDDR), and frequency resolved raman (FRR).⁷⁻¹¹ Among these technologies, SThM and TDTR are the dominating ones while only TDTR provides quantitative calculation results of thermal conductivity.⁷ The capability of SThM could be far beyond once quantitative measurement becomes possible. For example, thermal conductivity distribution of heterogeneous materials can be precisely mapped at nanometer resolution; thermal conduction across nanointerface of composites can be quantified.

SThM was developed by Clayton C. Williams and H. Kumar Wickramasinghe in 1986.¹² SThM measurement is usually carried out on atomic force microscopy (AFM) platform with additional thermal measurement accessories including thermal tip. During measurement, thermal tip scans across sample surface and captures the feedback signal to get

analyzable information of local thermal properties.¹³⁻¹⁶ Because of a unique combination of high spatial resolution and thermal property, SThM has been widely used to characterize thermal property of various materials during past two decades.¹⁷⁻²⁰ It is widely accepted that SThM results can be used to tell the relative difference of materials at different regions.²¹⁻²⁵ However, the quantification profile of the measurement is still not available yet. By combining other techniques such as spatially resolved Raman spectroscopy or ultra-high vacuum scanning thermal microscopy, quantitative profile of thermal conductivity can be achieved while the experimental setup is much more complicated.²⁶⁻²⁹ Until now, there is no established methods to obtain thermal conductivity via SThM. Here, the major challenge comes from the varied thermal resistance (or called “air gap”) at tip-sample interface, which greatly influences the overall reading of thermal signal. Digging into the working principle of SThM, the thermal feedback signal is determined by the heat dissipation through sample and heat dissipation across tip-sample interface.^{8, 26, 28, 30-32} The “air gap” existing between thermal tip and sample surface is formed due to the intrinsic roughness of the contacting surface, which is the major obstacle of quantitative calculation of thermal conductivity with SThM.^{8, 33} The “air gap” can be seen as a thermal resistor which is influenced by many factors at the interface including but not limit to surface roughness, hardness, intrinsic thermal conductivity of sample, contact force, *etc.* The “air gap” is the key area needs to be better understood for bridging the communication between tip and sample surface. However, a quantitative method is still not available yet to predict the thermal contact resistance (TCR) at interface. Therefore, a correlation between probe current and thermal conductivity of materials cannot be established and thus SThM is mostly used for qualitative analysis. Once TCR at interface can be assessed, a direct relationship between thermal probe current and thermal conductivity becomes possible which provides a unique tool for measuring in-plane thermal conductivity distribution in nanoscale domain.

Here, we developed a microscopic model that well describes the interfacial thermal resistance between thermal probe and sample surface during SThM measurement. By using this model, the probe current and thermal conductivity of testing specimen can be well correlated and thus quantitative thermal conductivity analysis by SThM becomes possible. This model is developed based on a comprehensive understanding of intrinsic interfacial features including sample roughness and micro-hardness, contacting force as well as the contacting area. Therefore, this model can be extended to study a wide range of material systems. In this work, two different models (linear and non-linear) are developed that quantitatively correlate the probe current and thermal conductivity for different material systems. Material surface feature needs to be considered for model selection. Thermal conductivity measurement on bulk samples is carried out to verify the predicted thermal conductivity from models based on SThM probe current. Three polymeric systems, epoxy, polydimethylsiloxane (PDMS) and polyvinyl alcohol (PVA) were selected and tested to verify the effectiveness of the models in predicting thermal conductivity. The results of this work not only provide a good understanding of heat conduction across the nanointerface between thermal probe and sample surface, but also offer a reliable method to obtain quantified thermal property at a scale down to nanometer range.

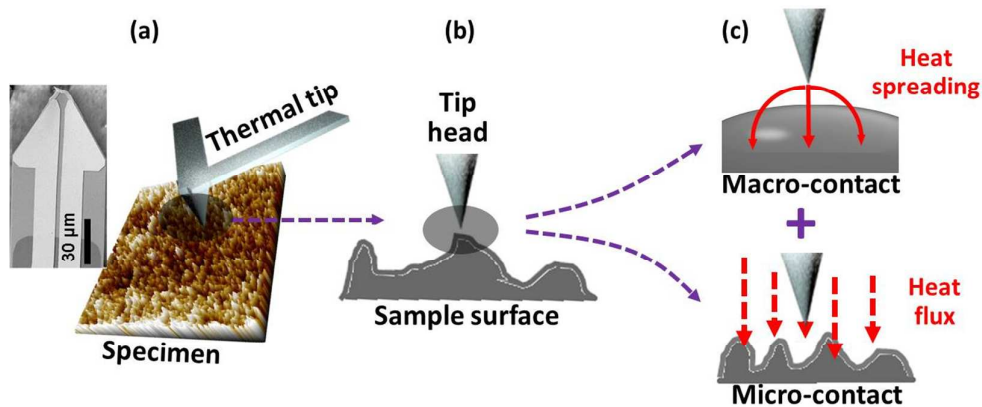
2. Modeling Part

2.1 Modeling of thermal contact resistance (TCR)

The main challenge of using SThM for thermal conductivity measurement is the quantification of TCR at tip-sample contacting interface. The “air gap” between thermal probe and sample surface is the main reason of TCR during scanning process, which behaves like a thermal contact resistor. Since the interfacial contact is affected by many factors, it is necessary to simply the contacting mode and then quantitatively describe it. Scheme 1a shows the contacting mode of thermal probe scanning on top of sample surface. Such

contacting mode is similar to the situation of two nonconforming rough surfaces described by M. Bahrami.³⁴ Here we have one rough surface and the other is smooth thermal probe surface (Scheme 1b). The rough sample surface can be further simplified into two parts based on heat transfer mode at the interface, *i.e.* heat spreading of macro-contact and heat flux of micro-contact. Macro- and micro-contact resistances are the two major forms of TCR at the interface of two contact surfaces.³⁵ The total contact resistance (R_{cont}) can be calculated by the summation of macro-contact resistance (R_{ma}) and micro-contact resistance (R_{mi}), equation (1):

$$R_{cont} = R_{ma} + R_{mi} \quad (1)$$



Scheme 1. (a) “Air gap” between thermal tip and sample surface; (b) real contact situation between tip head and sample surface; (c) simplified contact modes: macro-contact and micro-contact. Cantilever is made by silicon nitride with a size of $150 \times 60 \times 0.4 \mu\text{m}$. Resistor metal is composed of NiCr and Pd and track metal is composed of NiCr and Au. The radius of thermal tip is $\sim 100 \text{ nm}$ with a height around $10 \mu\text{m}$. Spring constant is 0.25 N/m .

R_{ma} is majorly attributed to the thermal spreading resistance (R_s),³⁴ which is formed due to the non-uniform distribution of heat at heated side and consequently insufficient heat transfer from the heat source.^{36, 37} It is defined as the temperature difference between the heat source and contact area divided by the heat flux, equation (2):

$$R_s = dT/Q \quad (2)$$

To calculate R_s , Cooper³⁸ proposed a rigorous but simple method by using isothermal flux tube model. In this model, R_s is a function of spreading resistance factor (φ), radius of macro-contact (a) and effective thermal conductivity (k), equation (3):

$$R_s = \varphi(\varepsilon)/2k_e a \quad (3)$$

where $\varphi(\varepsilon) = (1-a/b)^{1.5}$, b is the radius of flux tube, $k_e = 2kk_t/(k+k_t)$. In our tip-sample system, a is tip radius, b is sample size and k_e is the effective thermal conductivity across tip-sample interface. Due to the much lower thermal conductivity of the selected polymers compared to tip (made of NiCr and Pd), k_e can be simplified as $k_e = 2k$. Since tip radius is much smaller than sample size ($a \ll b$), the equation for R_{ma} can be further simplified, equation (4):

$$R_{ma} = R_s = \frac{\varphi(\varepsilon)}{2k_e a} = \frac{(1-a/b)^{1.5}}{2k_e a} = \frac{1}{4ka} \quad (4)$$

For micro-contact R_{mi} , Bahrami³⁴ proposed a model by combining Yovanovich³⁹ empirical equation, equation (5):

$$R_{mi} = \frac{2H}{\pi k_e F} \frac{\sigma}{m} = \frac{H}{\pi k F} \frac{\sigma}{m} \quad (5)$$

where H is micro-hardness, σ is effective roughness, F is contact force and m is effective slope of tip and sample. In this work, H is calculated via Oliver and Pharr⁴⁰ model by atomic force microscopy (AFM) based nanoindentation method.^{41, 42} 16 local harness values are measured, and the reported micro-hardness is the average of the 16 measurements. $\sigma =$

$\sqrt{\sigma_{\text{sample}}^2 + \sigma_{\text{tip}}^2}$, where σ_{sample} is sample surface roughness measured by AFM and σ_{tip} is considered as 0 (assuming smooth tip surface). F is contact force of tip on sample surface.

$m = \sqrt{m_{\text{sample}}^2 + m_{\text{tip}}^2}$, where m_{sample} is sample slope obtained from original AFM 3D topography images without flattening process and m_{tip} is considered as 0 (assuming flat tip surface).

After combining macro- and micro-contact thermal resistance, R_{cont} can be written in equation (6), where R_{cont} is related to thermal conductivity, micro-hardness, roughness of the prepared sample, slope of sample surface and the loading force of tip during measurement.

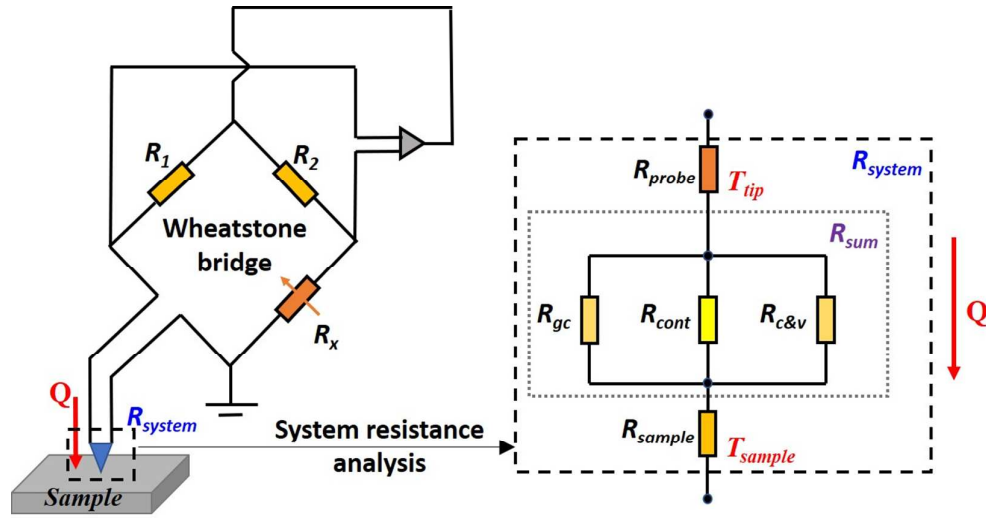
$$R_{cont} = R_{ma} + R_{mi} = \frac{1}{4ka} + \frac{H}{\pi k F} \frac{\sigma}{m} \quad (6)$$

2.2 Modeling of SThM

SThM uses nanofabricated thermal probes with resistive elements to achieve high spatial and thermal resolution with a unique signal detection configuration. Based on the working principle, two different measurement modes can be used in SThM: temperature contrast mode (TCM) and conductivity contrast mode (CCM).⁴³⁻⁴⁶ In TCM mode, the thermal probe is heated at a constant current and then it is functioning as a resistance thermometer. Specifically, as the thermal probe scans through a surface with non-uniform distribution of thermal conductivity, the probe temperature varies with the heat flux across tip/surface interface that is determined by the thermal conductivity of contacting area. In the CCM mode, thermal probe is used as a resistive heater and sufficient energy is applied to keep a constant probe surface temperature. Probe current is measured as an index of thermal conductivity.^{19, 47-49} In this work, CCM mode was adopted for the systematic study.

Scheme 2 presents the diagram of the SThM CCM mode (Wheatstone bridge) and analysis of the thermal resistances in the system. The Wheatstone bridge feedbacks, adjusts, and balances the bridge voltage to measure probe current. The fixed resistors R_1 and R_2 form one arm of the bridge while the rheostat R_x and the R_{system} form the other arm of the bridge. Since R_1 and R_2 are fixed, R_x can be adjusted to balance the bridge once R_{system} changes. The output voltage is in direct proportion to the current through the bridge and thus the probe current. R_{system} is the summation of R_{probe} , R_{sum} and R_{sample} . R_{probe} can be neglected since it is made of highly conductive metals and its thermal resistance is much smaller than the other

two. R_{sum} is contributed by three resistance parts in parallel connection: gas conduction (R_{gc}), contact (R_{cont}) and convection and radiation ($R_{c&v}$). In most cases, R_{gc} and $R_{c&v}$ are orders of magnitude higher than R_{cont} . Therefore, R_{sum} can be considered approximately the same as R_{cont} .



Scheme 2. Diagram of CCM mode of SThM and systematic analysis of thermal resistance across tip/sample surface interface.

Considering the total system energy balance, the energy ($Q = UI$, U is the voltage of Wheatstone bridge and the I is the probe current) into electrical circuit system will be dissipated through two different ways: one is heat generation at the fixed resistors (Q_F) and the other is heat flux through the tip/surface contacts (Q_R), equation (7):

$$Q = UI = Q_F + Q_R \quad (7)$$

According to Fourier's law, Q_R can be written by equation (8):

$$Q_R = \Delta T / R \quad (8)$$

where $\Delta T = T_{tip} - T_{sample}$, $R = R_{sample} + R_{cont}$ (T_{tip} is the temperature of tip; T_{sample} is the temperature of sample surface). R_{sample} can be obtained by moving heat source method^{50, 51}: $R_{sample} = \frac{1}{\pi r_0 k}$, r_0 is radius of heat source which is equal to the tip radius (100 nm) and k is the thermal conductivity of sample. Combining equations (7) and (8) into equation (9):

$$Q = UI = \frac{(T_{tip}-T_{sample})}{\frac{1}{\pi r_0 k} + R_{cont}} + Q_F \quad (9)$$

By substituting equation (6) into equation (9), equation (10) can be obtained

$$I = \frac{(T_{tip}-T_{sample})}{U} \frac{1}{\frac{1}{\pi r_0 k} + \frac{1}{4ka} + \frac{H}{\pi k F m}} + \frac{Q_F}{U} \quad (10)$$

Since T_{tip} is maintained at a constant temperature during testing, $T_{tip}-T_{sample}$ will remain a constant. This has also been verified from experiment since the change of probe current versus the base input current is less than 0.56%. That is said, the temperature change of the T_{tip} can be neglected and therefore $T_{tip}-T_{sample}$. Meanwhile, the applied voltage (U) is fixed during experiment. At specified experimental conditions, equation (10) can be rewritten into equation (11):

$$I = \frac{A}{\frac{1}{\pi r_0 k} + \frac{1}{4ka} + \frac{H}{\pi k F m}} + B \quad (11)$$

where $A = \frac{(T_{tip}-T_{sample})}{U}$ and $B = \frac{Q_F}{U}$, A and B are constants relating to instrument parameters. From equation (11), the probe current I is related to the thermal conductivity (k), micro-hardness (H), sample surface roughness (σ), loading force of tip (F) and slope of sample and tip (m). H , σ and m can be characterized by AFM, F is a set value that can be adjusted as desired. Thus, a relationship between probe current I and thermal conductivity k can be constructed after identifying all other parameters in equation (11). In this work, three polymer systems, polydimethylsiloxane (PDMS), epoxy and polyvinyl alcohol (PVA), were employed to verify the model in correlating probe current and thermal conductivity by considering the surface features at nanoscale.

3. Experimental

3.1 Materials

PDMS (sylgard-184) was provided by Dow Corning. Epoxy resin (826 RS, 178-186 g/eq) was purchased from HEXION Inc. Curing agent (JEFFAMINE T403, max 0.25 wt%

water) was provided by Huntsman Corporation. PVA powder (Mw: 14600~18600, 99+% hydrolyzed) was purchased from Sigma-Aldrich. Cobalt nitrate ($\text{Co}(\text{NO}_3)_2$, >98%), Iron chloride (FeCl_2 , >97%), Zinc chloride (ZnCl_2 , >97%) were purchased from Sigma-Aldrich. All chemicals were used as received without further purification.

PDMS films were prepared by mixing different ratios of base monomer and curing agent. The percentage of the curing agent is fixed at 2, 5, 10, 20, 40 and 50 wt%. PDMS base monomer and curing agent were stirred for 20 mins at room temperature and then cured in a petri dish for 4 hours at 80 °C. PDMS samples were named PDMS-X (X=2, 5, 10, 20, 40 and 50%).

Epoxy films were prepared by mixing different loading percentages of curing agent: 10, 20, 30, 40 and 50 wt%. The well mixed specimen was placed in a rubber mold for curing. Before curing, samples were degassed in a vacuum oven for 30 mins. Then it was cured at 80 °C for 4 hours in a regular oven. Epoxy samples were named Epoxy-X (X=10, 20, 30, 40 and 50%).

PVA aqueous solution was prepared at concentration of 8.0 wt%. PVA/salt solutions were prepared by a mixture of PVA solution and salt solution ($\text{Co}(\text{NO}_3)_2$, FeCl_2 , ZnCl_2) at fixed molar ratio of 1:0.05. All the solutions were placed in an oven and dried at 40 °C (3 days) for thin film preparation. Samples were named PVA, PVA-Co, PVA-Fe and PVA-Zn, respectively.

3.2 Characterization

SThM characterizations were performed with Park System XE7 Atomic Force Microscopy. The thermal tip is made of silicon base and thermally grown SiO_2 cantilever. Base dimension is 2× 3 mm and cantilever dimension is 150×60×1 μm. The resistor metal is made of 5 nm NiCr and 40 nm Pd. Tip height is 12 μm and tip radius is around 100 nm. The resistance of the tip is around 200-600 Ω. Thermal coefficient of resistivity is about 1 Ω/°C.

Spring constant is 0.45 N/m and resonance frequency is 48 KHz. The pre-setting probe current was 1.20 mA. Micro-hardness was characterized by nanoindentation with AFM. Thermal probe was used to collect nanoindentation data that ensured the captured current signal and measured micro-hardness are from exactly the same region. The micro-hardness results were analyzed by Olive and Pharr method.⁴⁰ Surface roughness was analyzed from surface topography. Slope value was determined by the calculation of line profile via AFM 3D image without flattening process. The loading force is set at 1.97, 3.97 and 5.97 nN, respectively. Thermal conductivity measurement of polymer films was carried out at room temperature by using TCi analyzer (C-Therm, Canada).

4. Results and Discussion

4.1 Model testing and simplification

PDMS-20% and Epoxy-30% are selected to test the model and generate useful information for further model validation. Figure 1 shows the microscopic characterization of both PDMS-20% and Epoxy-30% by AFM-SThM. Figure 1(a1) gives original SThM probe current image which is used to calculate the average probe current of the entire surface. The average probe current value is shown inside the scanning image. Figure 1(b1) shows 3D topography image without flattening process and the corresponding height line profile with calculated slope value m labeled inside the figure. Figure 1(c1&d1) are topography and thermal mapping images of PDMS-20%. Similar characterizations are carried out on Epoxy-30% and the results are presented in Figure 1(a2-d2). All the parameters used for model testing and calculated R_{ma} and R_{mi} in both PDMS and Epoxy are summarized in Table 1.

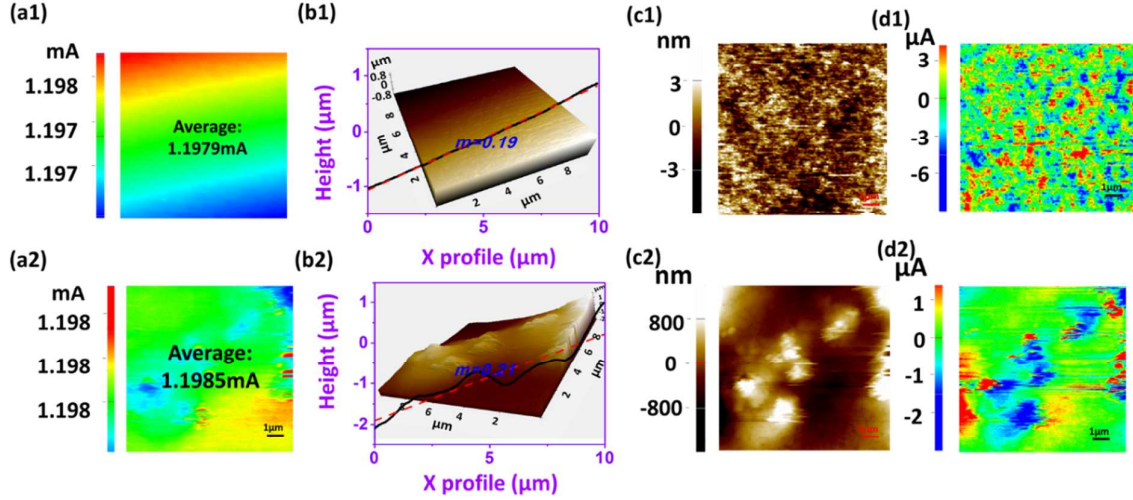


Figure 1. Characterization of (a1-d1) PDMS-20% and (a2-d2) epoxy-30%. (a1&a2) original STHM probe current image, (b1&b2) AFM 3D image without flattening process, (c1&c2) AFM topography images, (d1&d2) STHM thermal mapping images.

Table 1. Summarized parameters for PDMS and epoxy systems.

Materials	k ($\text{Wm}^{-1}\cdot\text{K}^{-1}$)	a (nm)	H (kPa)	σ (nm)	F (nN)	m	R_{ma} (WK^{-1})	R_{mi} (WK^{-1})
PDMS-20%	0.203	100	25.6	1.37	1.97	0.19	1.23E7	1.47E5
Epoxy-30%	0.235	100	33.0	202.03	1.97	0.19	1.06E7	2.18E7

As seen in Table 1, R_{ma} is about two orders of magnitude larger than that of R_{mi} in PDMS-20%. Thus, the contribution of R_{ma} in TCR can be neglected for PDMS. That is, the R_{cont} can be considered the same as R_{ma} , which is only related to the thermal conductivity of sample and tip radius. Then, equation (11) can be rewritten into equation (12) for PDMS, where a linear relationship between probe current I and thermal conductivity k can be found:

$$I = \frac{A}{\frac{1}{\pi r_0 k} + \frac{1}{4ka}} + B = A \cdot C \cdot k + B \quad (12)$$

$$C = \frac{4a\pi r_0}{4a + \pi r_0} = \frac{4a\pi}{4 + \pi} \quad (r_0 = a)$$

Epoxy-30% shows different surface features as compared to PDMS-20%, especially the surface roughness as summarized in Table 1. The R_{mi} is in direct proportion to the surface

roughness (equation 5) that leads to a comparable R_{ma} and R_{mi} . Therefore, none of these terms in equation (10) can be neglected in epoxy system.

Back to the heat transport principle between two solid materials: roughness, hardness and contact force are the three major factors influencing the TCR at interface.⁵²⁻⁵⁵ In this work, contact force is a pre-setting constant value during the test. The hardness value is at the same order of magnitude for both PDMS and Epoxy systems. The varied surface roughness is the major reason for the dramatically different R_{mi} in both materials. These results indicate that surface roughness could be the dominating factor for TCR. Sample surface with a small roughness leads to a linear relationship between probe current and thermal conductivity. While a surface with large roughness, probe current is related to thermal conductivity and other factors as well (mainly micro-hardness and roughness).

4.2 Model validation

In section 4.1, two different models were developed for PDMS and epoxy systems, respectively, to correlate probe current and thermal conductivity by analyzing the interfacial TCR. To verify the models, more specimens with varied base/curing agent ratios were tested. Figures 2&3 summarize the features of PDMS and epoxy resins characterized by AFM and SThM. In general, the surface roughness of all the PDMS samples is much smaller than that of epoxy, as evidenced by the scales of topography images in Figure 2(c1-c6) and Figure 3(c1-c5). It is worth noticing that the topography pattern of the samples shows certain similarity to the pattern of probe current distribution. This is more obvious in epoxy samples where larger surface roughness was observed. Such similar pattern of topography and probe current indicates the remarkable influence of surface geometry on interfacial thermal transport. According to the working principle of SThM, topography capturing system and probe current signal feedback loop are two independent channels and they are not supposed to interfere with each other. Because probe current is a result of the combined action of

sample thermal conductivity and R_{cont} , the only explanation for the topography-related probe current distribution is that the heat flux caused by TCR is large enough and poses great influence on the final observation in thermal image. In other words, the feedback signal is mostly contributed by the heat flux of tip-sample interface rather than from the sample itself. Such results are in good agreement with literature reports from other researchers.^{28, 56} Based on the proposed model in this work, larger roughness value means higher TCR and thus lower probe current. For PDMS system, the surface roughness is much smaller (<2 nm) and no obvious correlation can be found between topography image and thermal image. Thus, probe current is randomly distributed without any specific patterns. All the samples show similar slope value (m) of around 0.2. The small difference of m values is not expected to impact further calculation significantly.

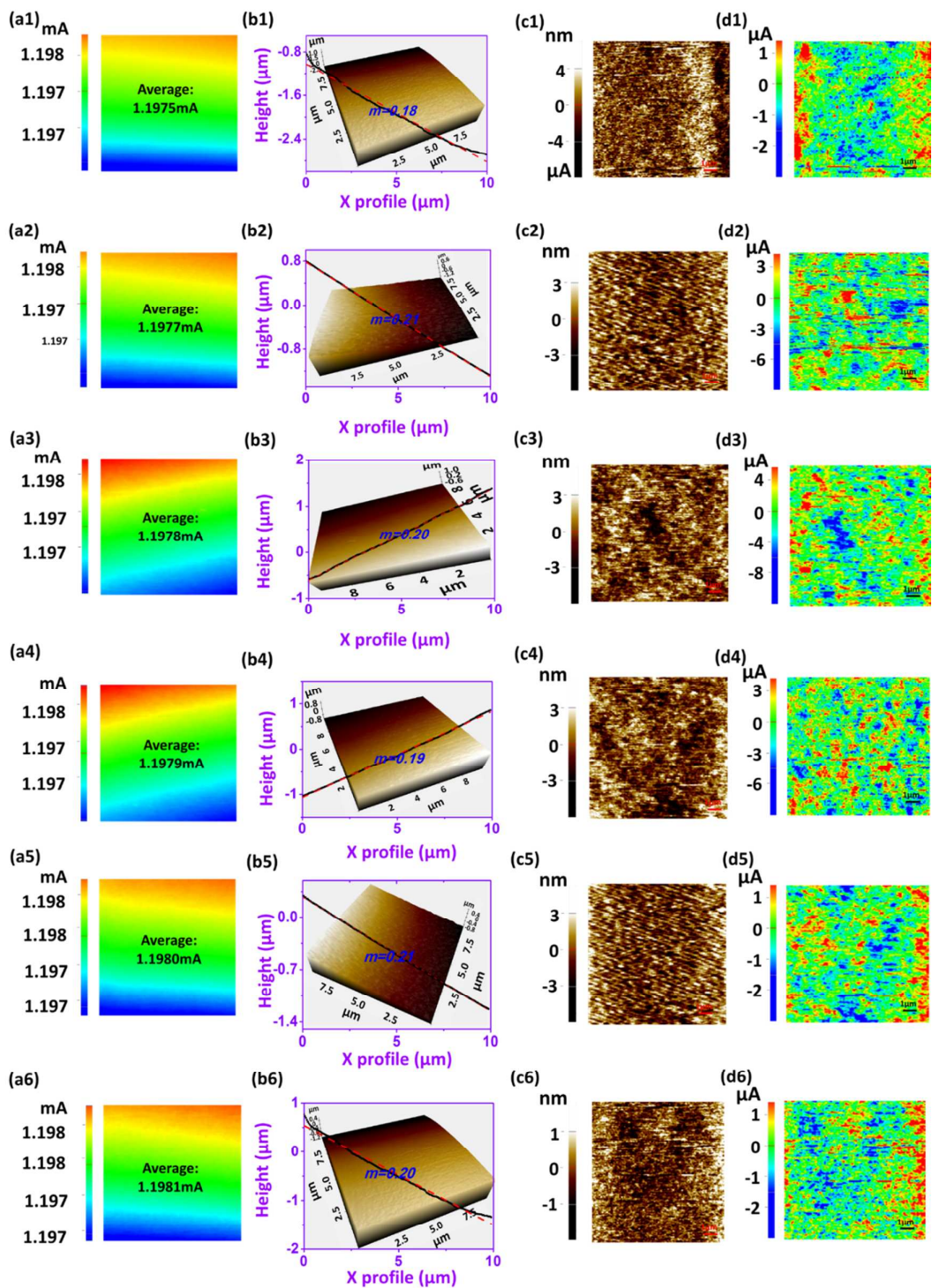


Figure 2. AFM and SThM characterization of PDMS. (a1-a6) original SThM probe current image, (b1-b6) AFM 3D image without flattening process, (c1-c6) AFM topography images, (d1-d6) SThM thermal mapping images. 1-6 means the increasing loading of curing agent in PDMS: 2, 5, 10, 20, 40 and 50 wt%.

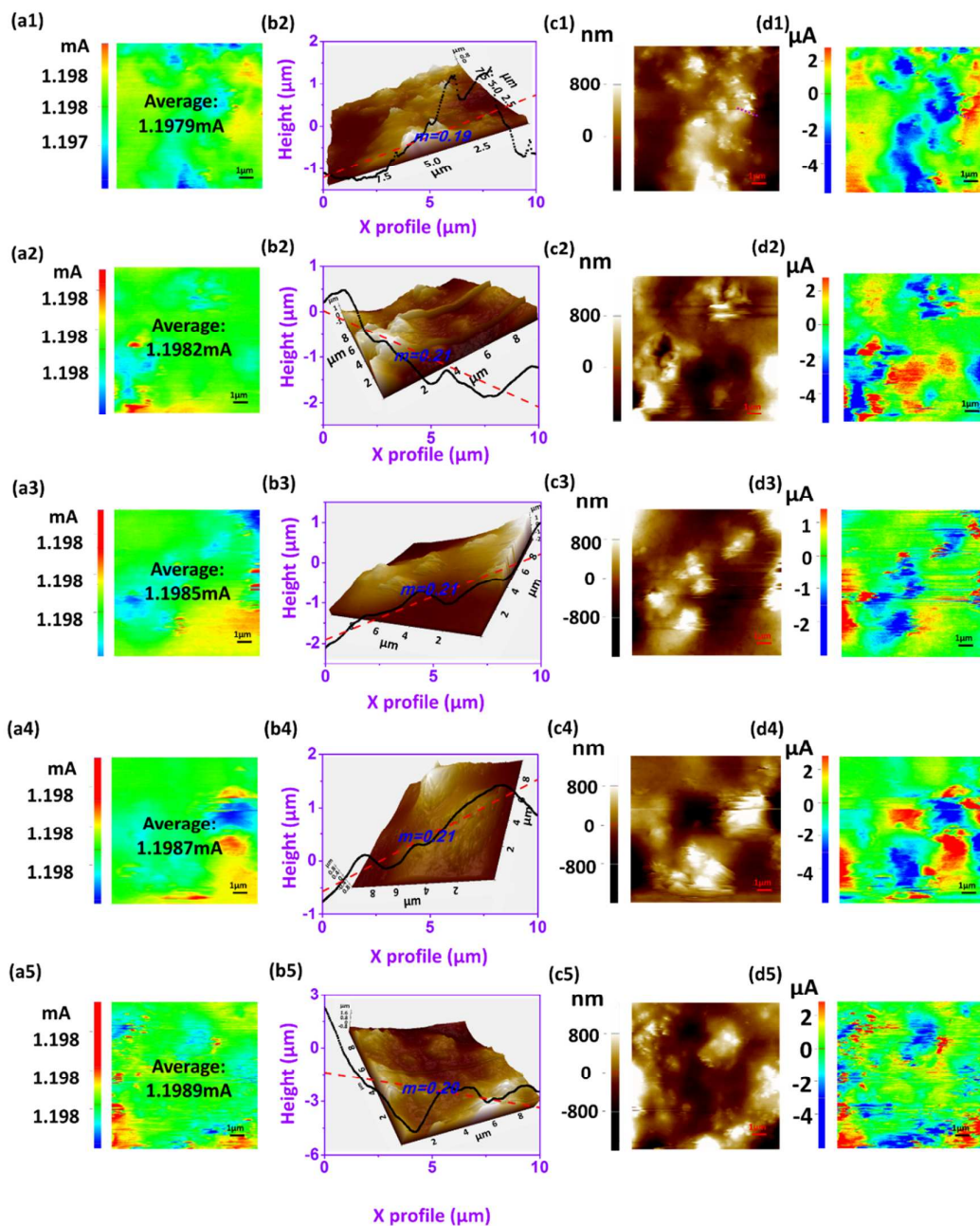


Figure 3. AFM and SThM characterization of epoxy. (a1-a5) original SThM probe current image, (b1-b5) AFM 3D image without flattening process, (c1-c5) AFM topography images, (d1-d5) SThM thermal mapping images. 1-6 means the increasing loading of curing agent in epoxy: 10, 20, 30, 40 and 50 wt%.

The probe current and bulk thermal conductivity of PDMS are measured by SThM CCM mode and TCi respectively, Figure 4(a&b). Both of them increase with increasing load percentage of curing agent. Figure 4(c&d) present the micro-hardness and surface roughness

as a function of the percentage of curing agent, where a gradual increase of both parameters was observed. It should be noticed that the variation of the hardness and roughness is still at the same level of magnitude. With that, equation (12) can be used for all the six PDMS samples and thus it is expected that the probe current and thermal conductivity of materials should follow a linear relationship. To verify the model, probe current against thermal conductivity was plotted in Figure 4(e). Since the variation of probe current is very small, the differentiation of the readings becomes difficult. Therefore, a revised probe current (I^*) was used in this work and the data was replotted in Figure 4(f):

$$I^*(\mu A) = \frac{I(nA) - 1.19 \times 10^6 nA}{1000}$$

Figure 4(f) shows a highly linear relationship ($R^2 > 0.99$) between I^* and thermal conductivity. Such results demonstrate a solid linear correlation between microscale probe current and macroscale thermal conductivity. The proposed model well describes such relationship and can be extended to predict thermal conductivity based on microscale measurements.

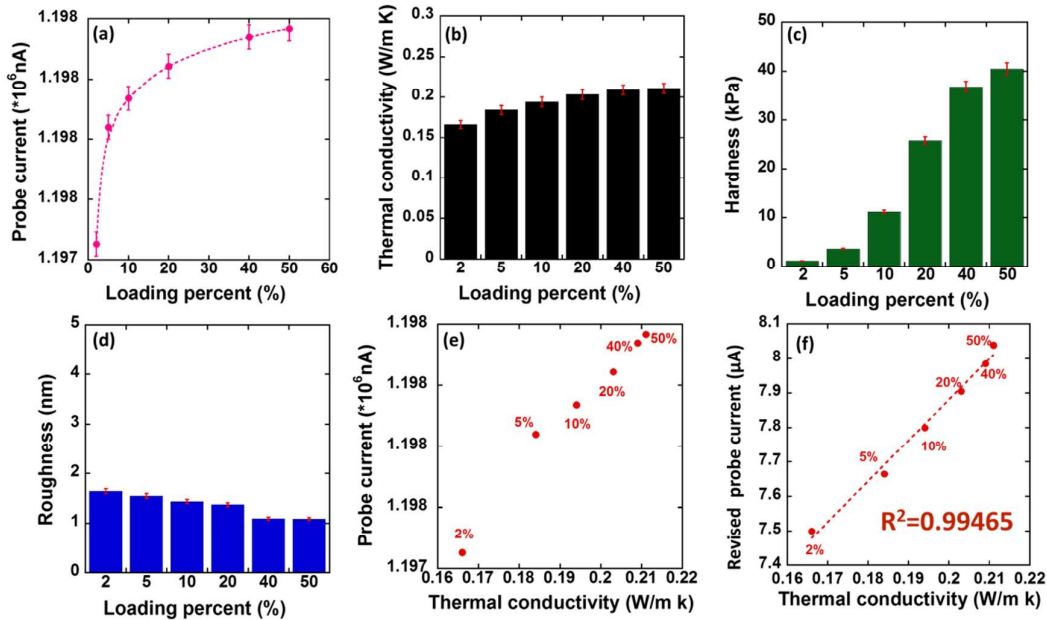


Figure 4. Parameters used for calculation in PDMS systems. (a) probe current, (b) thermal conductivity, (c) micro-hardness, (d) roughness, (e) probe current vs. thermal conductivity, (f) revised probe current vs. thermal conductivity and its linear fitting.

Similar to the PDMS system, Figure 5(a-d) summarize the characterization results of epoxy system. Compared to 30% curing agent system, both micro-hardness and roughness values of the other 4 epoxy samples are at the same order of magnitude. Therefore, the model cannot be simplified into linear form and equation (11) is used to model tip-surface thermal transport for epoxy. Figure 5(e) provides a relationship between probe current and thermal conductivity, which does not follow a linear pattern. Since micro-contact resistance cannot be neglected in equation (11), probe current I is not only related to thermal conductivity, other parameters should be considered as well. Taking the instrument parameters A and B from PDMS (A is slope, and B is intercept from the linear fitting) into epoxy model, a simplified relationship can be constructed between probe current and thermal conductivity. A good consistency of measured and calculated thermal conductivity can be found with less than 5% error, Figure 5(f).

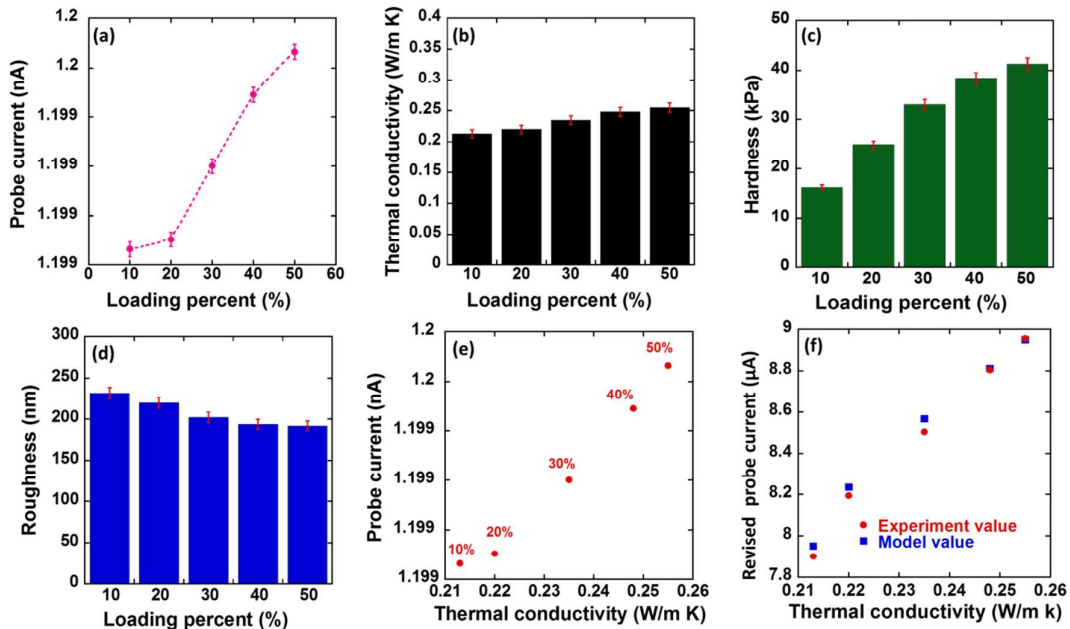


Figure 5. Parameters used for calculation in epoxy systems. (a) probe current, (b) thermal conductivity, (c) micro-hardness, (d) roughness, (e) probe current vs. thermal conductivity, (f) comparison of modeling and experiment results for revised probe current.

All the previous measurements are carried out at a loading force of 1.97 nN. The variation of loading force will change the interfacial contact and thus heat transport across the contacting interface. The robustness of the developed models needs to be tested at different loading force conditions. In this work, two other sets of loading forces are selected: 3.97 and 5.97 nN. The probe currents are collected at specified loading force conditions on all the samples. At the same time, the probe current is calculated from the developed models by substituting the force value. Figure 6(a) gives the comparison of revised probe current from both experiment and model prediction for PDMS at three different loading force conditions. It is observed that majority of the data points are overlapped at each loading percent indicating the negligible influence of loading force on the probe current measurement of PDMS as well as the robustness of the model at different testing conditions. These results could be expected since loading force only affects the R_{mi} in the model and R_{mi} can be neglected for PDMS system. As a result, the changes of loading force F do not influence the probe current measurement. Figure 6(b) shows the comparison of experiment/model probe current values for epoxy. In general, the model and experimental results follow a very similar trend at different loading forces indicating the good adaptability of the epoxy model. However, the amplitude of probe current increases with increasing loading force. By increasing loading force, a better interfacial contact can be expected especially on a rough surface. As a result, the thermal resistance at the interface can be reduced by a tight contact and thus larger probe current across the interface. In the developed epoxy model, the increase of loading force F decreases the term of R_{mi} and this increases the probe current I . Based on these results, it can be concluded that the two models developed in this work are reliable to correlate probe current and thermal conductivity for polymer materials with different surface features (low roughness and high roughness).

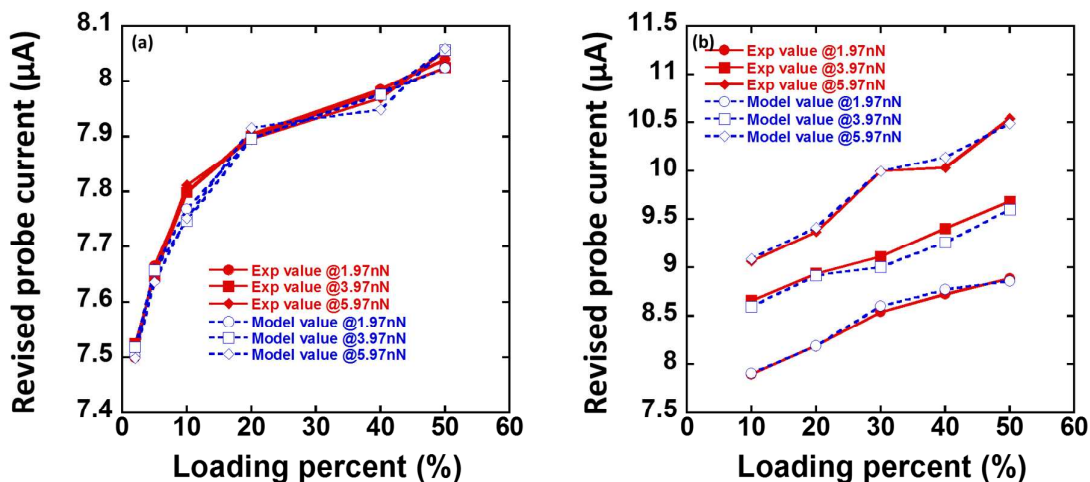


Figure 6. (a) Comparison of revised probe current by experiment and revised probe current by model under different loading force for PDMS system, (b) comparison of revised probe current by experiment and revised probe current by model under different loading force for epoxy system.

4.3 Model extrapolation with PVA and doped PVA

To further verify the effectiveness of the model to be used for other types of polymeric materials, PVA and doped PVA (PVA-Co, PVA-Fe and PVA-Zn) samples were employed in this work. The AFM and SThM characterization results are summarized in Figure 7(a-d). It is apparent that PVA system follow a similar pattern as PDMS, both of their surface roughness is of around a few nanometers. Therefore, the linear model (equation 11) can be applied for the PVA system. Figure 8(a-e) show the characterization results of the PVA based samples. Since the thermal conductivity of PVA samples is much larger than that of PDMS, extrapolation method is used here to predict the thermal conductivity. The predicted thermal conductivity from the model is marked with cross symbol on the extrapolated line and the corresponding experimental results are plotted as well. The experimental results are all closely distributed near the predicted values, Figure 8(f). All these results confirm the robustness of the developed model in predicting thermal conductivity in a wide range of polymeric materials.

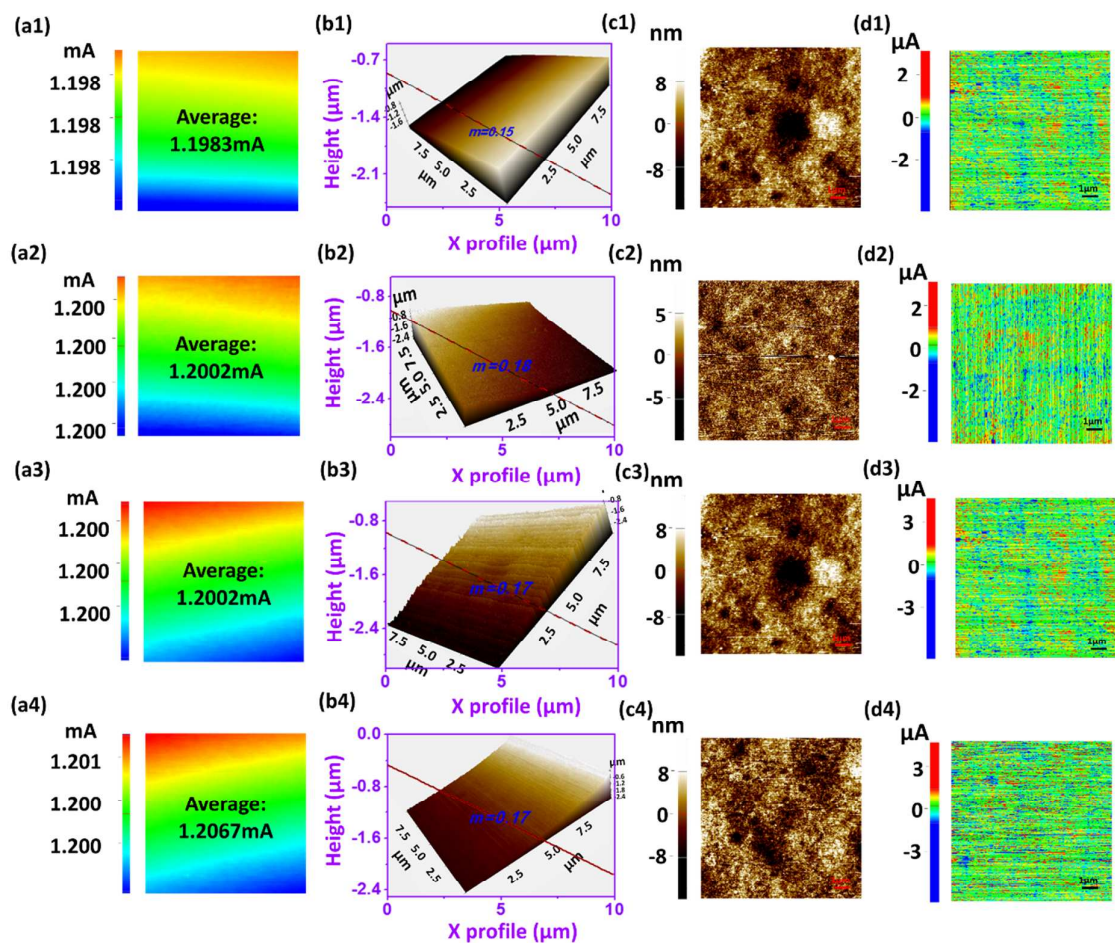


Figure 7. AFM and SThM characterization of PVA-salt systems (a1-a4) original SThM probe current image, (b1-b4) AFM 3D image without flattening process, (c1-c4) AFM topography images, (d1-d4) SThM thermal mapping images. 1-4 corresponds to PVA, PVA-Co, PVA-Fe and PVA-Zn, respectively.

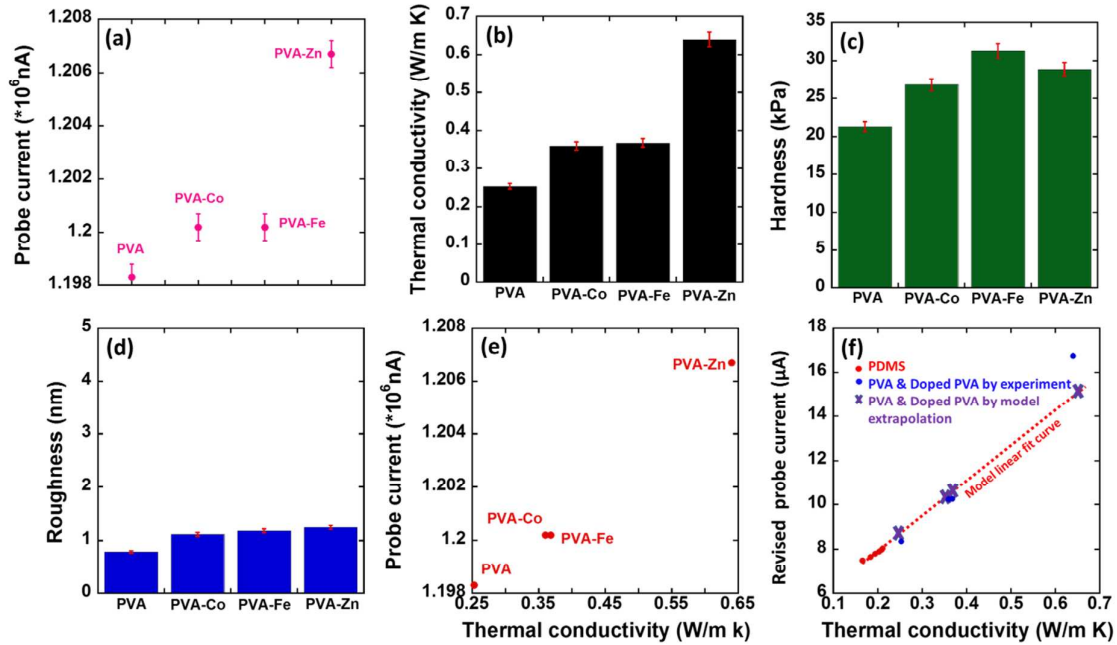


Figure 8. Parameters used for calculation in PVA-salt systems. (a) probe current, (b) thermal conductivity, (c) micro-hardness, (d) roughness, (e) probe current vs. thermal conductivity, (f) Comparison of revised probe current values of PVA systems by experiment and model extrapolation.

4. Conclusions

In summary, this work derives a mathematical model that well correlates the SThM probe current and bulk thermal conductivity of polymeric materials. The key challenge of this work-quantification of thermal contact resistance (TCR), is addressed by implementing micro-structural features at the interface such as surface roughness, hardness, *etc.* Two different models, linear and non-linear, are successfully developed which can be used to predict thermal conductivity of materials by measuring SThM surface probe current. Surface roughness is the major criteria for model selection. That is, linear model fits samples with smooth surface while non-linear model applies to samples with rough surface. Both models provide satisfactory prediction results in three polymeric material systems: PDMS, epoxy and PVA. Changing the loading force does not affect the effectiveness of the model, which expands the applicability of the developed models in wider range of materials. Moreover, the

model has been tested valid when extrapolated to predict thermal conductivity beyond the range of model development. This work developed a simple but rigorous method to mathematically describe the thermal contact resistance at tip/surface interface and offers reliable models to enable quantitative characterization of thermal conductivity by SThM. This unique feature endows SThM new capability in quantitative thermal analysis with spatial resolution down to nanometer, which is promising to quantify the thermal conduction across interfaces within composites, multi-layer membranes, microelectronics, *etc.*

ACKNOWLEDGEMENTS

Acknowledgement is made to the Donors of the American Chemical Society Petroleum Research Fund (#55570-DNI10), National Science Foundation (CBET-1603264). Partial support from the start-up fund of The University of Akron is also acknowledged.

CONFLICTS OF INTEREST

The authors declare no conflict of interest.

REFERENCES

1. B. Song, Y. Ganjeh, S. Sadat, D. Thompson, A. Fiorino, V. Fernández-Hurtado, J. Feist, F. J. Garcia-Vidal, J. C. Cuevas and P. Reddy, *Nat. Nanotechnol.*, 2015, **10**, 253-258.
2. Y. Zhang, H. Han, N. Wang, P. Zhang, Y. Fu, M. Murugesan, M. Edwards, K. Jeppson, S. Volz and J. Liu, *Adv. Funct. Mater.*, 2015, **25**, 4430-4435.
3. R. Von Herzen and A. Maxwell, *J. Geophys. Res.*, 1959, **64**, 1557-1563.
4. K. A. Borup, J. De Boor, H. Wang, F. Drymiotis, F. Gascoin, X. Shi, L. Chen, M. I. Fedorov, E. Müller and B. B. Iversen, *Energy Environ. Sci.*, 2015, **8**, 423-435.
5. H. Ji, D. P. Sellan, M. T. Pettes, X. Kong, J. Ji, L. Shi and R. S. Ruoff, *Energy Environ. Sci.*, 2014, **7**, 1185-1192.
6. J. D. Richards, *IEEE Electr. Insul. Mag.*, 1988, **4**, 23-32.
7. M. D. Losego, M. E. Grady, N. R. Sottos, D. G. Cahill and P. V. Braun, *Nat. Mater.*, 2012, **11**, 502-506.

8. K. Kim, B. Song, V. Fernández-Hurtado, W. Lee, W. Jeong, L. Cui, D. Thompson, J. Feist, M. H. Reid and F. J. García-Vidal, *Nature*, 2015, **528**, 387-391.
9. C. Li, S. Xu, Y. Yue, B. Yang and X. Wang, *Carbon*, 2016, **103**, 101-108.
10. L. Su and Y. Zhang, *Appl. Phys. Lett.*, 2015, **107**, 071905.
11. S. Wheaton, R. M. Gelfand and R. Gordon, *Nat. Photonics*, 2015, **9**, 68-72.
12. C. Williams and H. Wickramasinghe, *Microelectron. Eng.*, 1986, **5**, 509-513.
13. D. Halbertal, J. Cuppens, M. B. Shalom, L. Embon, N. Shadmi, Y. Anahory, H. Naren, J. Sarkar, A. Uri and Y. Ronen, *Nature*, 2016, **539**, 407-410.
14. S. Huxtable, D. G. Cahill, V. Fauconnier, J. O. White and J.-C. Zhao, *Nat. Mater.*, 2004, **3**, 298-301.
15. A. Böker, Y. Lin, K. Chiapperini, R. Horowitz, M. Thompson, V. Carreon, T. Xu, C. Abetz, H. Skaff and A. Dinsmore, *Nat. Mater.*, 2004, **3**, 302-306.
16. L. Cui, W. Jeong, V. Fernández-Hurtado, J. Feist, F. J. García-Vidal, J. C. Cuevas, E. Meyhofer and P. Reddy, *Nat. Commun.*, 2017, **8**, 14479.
17. Y. Li, N. Mehra, T. Ji, X. Yang, L. Mu, J. Gu and J. Zhu, *Nanoscale*, 2017, **10**, 1695-1703.
18. L. Shi, S. Plyasunov, A. Bachtold, P. L. McEuen and A. Majumdar, *Appl. Phys. Lett.*, 2000, **77**, 4295-4297.
19. L. Mu, Y. Li, N. Mehra, T. Ji and J. Zhu, *ACS Appl. Mater. Interfaces*, 2017, **9**, 12138-12145.
20. N. Mehra, L. Mu, T. Ji, Y. Li and J. Zhu, *Compos. Sci. Technol.*, 2017, **151**, 115-123.
21. V. Gorbunov, N. Fuchigami, J. Hazel and V. Tsukruk, *Langmuir*, 1999, **15**, 8340-8343.
22. X. Yan, Y. Imai, D. Shimamoto and Y. Hotta, *Polymer*, 2014, **55**, 6186-6194.
23. J. Christofferson, K. Maize, Y. Ezzahri, J. Shabani, X. Wang and A. Shakouri, *2007 International Conference on Thermal Issues in Emerging Technologies: Theory and Application*, 2007, 3-9.
24. P. D. Tovee and O. V. Kolosov, *Nanotechnology*, 2013, **24**, 465706.
25. I. Jo, I.-K. Hsu, Y. J. Lee, M. M. Sadeghi, S. Kim, S. Cronin, E. Tutuc, S. K. Banerjee, Z. Yao and L. Shi, *Nano Lett.*, 2010, **11**, 85-90.
26. G. B. M. Fiege, A. Altes, R. Heiderhoff and L. J. Balk, *J. Phys. D: Appl. Phys.*, 1999, **32**, L13.
27. A. Soudi, R. D. Dawson and Y. Gu, *ACS Nano*, 2010, **5**, 255-262.
28. K. Kim, J. Chung, G. Hwang, O. Kwon and J. S. Lee, *ACS Nano*, 2011, **5**, 8700-8709.
29. K. Kim, W. Jeong, W. Lee and P. Reddy, *ACS Nano*, 2012, **6**, 4248-4257.

30. A. Majumdar, *Annu. Rev. Mater. Sci.*, 1999, **29**, 505-585.
31. K. Kim, W. Jeong, W. Lee, S. Sadat, D. Thompson, E. Meyhofer and P. Reddy, *Appl. Phys. Lett.*, 2014, **105**, 203107.
32. A. Assy, S. Lefèvre and S. Gomès, *21st International Workshop on Thermal Investigations of ICs and Systems (THERMINIC)*, 2015, 1-5.
33. K. Yoon, G. Hwang, J. Chung, H. Goo Kim, O. Kwon, K. D. Kihm and J. S. Lee, *Carbon*, 2014, **76**, 77-83.
34. M. Bahrami, J. Culham, M. Yovanovich and G. Schneider, *J. Thermophys Heat Transfer*, 2004, **18**, 218-227.
35. R. S. Prasher and P. E. Phelan, *J. Appl. Phys.*, 2006, **100**, 063538.
36. Y. Muzychka, M. Yovanovich and J. Culham, *J. Thermophys Heat Transfer*, 2006, **20**, 247-255.
37. Y. Muzychka, M. Yovanovich and J. Culham, *J. Thermophys Heat Transfer*, 2004, **18**, 45-51.
38. M. Cooper, B. Mikic and M. Yovanovich, *Int. J. Heat Mass Transfer*, 1969, **12**, 279-300.
39. M. Yovanovich, *AIAA paper*, 1982, **81**, 83-95.
40. G. Pharr and W. Oliver, *MRS Bull.*, 1992, **17**, 28-33.
41. T. Young, M. Monclus, T. Burnett, W. Broughton, S. Ogin and P. Smith, *Meas. Sci. Technol.*, 2011, **22**, 125703.
42. K. Miyahara, N. Nagashima, T. Ohmura and S. Matsuoka, *Nanostruct. Mater.*, 1999, **12**, 1049-1052.
43. K. Kim, B. Song, V. Fernández-Hurtado, W. Lee, W. Jeong, L. Cui, D. Thompson, J. Feist, M. H. Reid and F. J. García-Vidal, *Nature*, 2015, **528**, 387-391.
44. L. Gross, *Nat. Chem.*, 2011, **3**, 273-278.
45. F. Guo, N. Trannoy and J. Lu, *Mater. Sci. Eng. A*, 2004, **369**, 36-42.
46. F. Guo, N. Trannoy and J. Lu, *Superlattices Microstruct.*, 2004, **35**, 445-453.
47. A. Dawson, M. Rides, A. S. Maxwell, A. Cuenat and A. R. Samano, *Polym. Test.*, 2015, **41**, 198-208.
48. A. Dawson, M. Rides, A. Cuenat and L. Winkless, *Int. J. Thermophys.*, 2013, 1-18.
49. Y. Bellouard, M. Dugan, A. A. Said and P. Bado, *Appl. Phys. Lett.*, 2006, **89**, 161911.
50. P. Dawson and S. Malkin, *J. Eng. Ind.*, 1984, **106**, 179-186.
51. Y. Gu, X. Ruan, L. Han, D. Zhu and X. Sun, *Int. J. Thermophys.*, 2002, **23**, 1115-1124.

52. M. Grujicic, C. Zhao and E. Dusek, *Appl. Surf. Sci.*, 2005, **246**, 290-302.
53. R. S. Prasher, *J. Heat Transfer*, 2001, **123**, 969-975.
54. M. Bahrami, M. M. Yovanovich and J. R. Culham, *Int. J. Heat Mass Transfer*, 2005, **48**, 3284-3293.
55. C. Fieberg and R. Kneer, *Int. J. Heat Mass Transfer*, 2008, **51**, 1017-1023.
56. L. Shi and A. Majumdar, *J. Heat Transfer*, 2002, **124**, 329-337.